Automated 3D segmentation of brain tumor using visual saliency

Subhashis Banerjee [a,b,*], Sushmita Mitra [a], B. Uma Shankar [a]

[a] *Machine Intelligence Unit, Indian Statistical Institute, Kolkata 700108, India*
[b] *Department of Computer Science and Engineering, University of Calcutta, Kolkata 700106, India*

A R T I C L E   I N F O

A B S T R A C T

There is a growing availability of medical imaging data from large number of patients, involving visual information from images in different modalities along with an associated complexity of the features of interest. It has therefore become essential to develop automated delineations to assist doctors and/or radiologists to analyze and speedup medical image understanding, preferably avoiding any user intervention. We present here a novel approach for the reliable, automated, and accurate 3D segmentation of brain tumors from multi-sequence magnetic resonance images. The tumor volume, detected using visual saliency, is evaluated in three-dimensions for small as well as large ROIs and/or VOIs. The proposed segmentation method is applied on the publicly available standard BRATS data set, and is found to achieve very high accuracy with good reliability (or repeatability) and robustness of results. Its robustness, is also investigated by measuring the impact of tumor size on segmentation accuracy, on the basis of the weak linear correlation. The results demonstrate that the segmentation generated by the proposed algorithm can be used for accurate, stable contouring, for both high- and low-grade tumors, as compared to several related state-of-the-art methods involving semi-automatic and supervised learning.

1. Introduction

The large size of medical image data, the complexity of Features Of Interest (FOIs), and the necessity to process these on time, both accurately and efficiently, are making the job of doctors and radiologists increasingly difficult. Therefore, it has become essential to develop automated delineation of Regions Of Interest (ROIs) and Volumes Of Interests (VOIs) to assist and speedup medical image understanding. Over the last decade cancer has become the deadliest killer worldwide [29]. By the time physical manifestations become evident, often metastasis has set in. This results in failure of local tumor control and poor patient prognosis. Radio-imaging, like magnetic resonance imaging (MRI), computed tomography (CT), positron emission tomography (PET), etc., constitutes one of the best noninvasive approaches for detection, diagnosis, treatment and prognosis of cancer. Particularly, the integration of diverse multimodal information in a quantitative manner provides specific clinical solutions for accurately estimating patient outcome [15].

Among different cancers of the brain, Glioblastoma multiforme (GBM) remains the most common and lethal form of primary tumor in adults with poor prognosis. The treatment and diagnosis of GBM is mostly guided by histopathology and

---

immunohistochemistry [18]. Repeated tumor biopsies in brain tumor is a very challenging problem. Therefore, noninvasive methods like imaging hold immense promise for assessing the state of the tumor. The high spatial resolution of MRI provides minute details of abnormalities, in terms of both shape and volume, in brain tumors. Due to its superior contrast in soft tissue structures, MRIs are routinely used for the diagnosis and characterization of tumors for the disease management. Particularly, MR imaging is very safe because it does not involve any exposure to radiation [29].

Medical experts manually segment different regions of interest (ROIs) for detection, diagnosis and planning of treatment. Automated medical image analysis, on the other hand, overcomes human bias and can handle large volumes of data. Variation in blood flow (perfusion) within a tumor causes variation in imaging features like necrosis and contrast. It was observed [45] that regions of tumor that are poorly perfused on contrast-enhanced $T1C$-weighted images may exhibit areas of low (or high) water content on $T2$-weighted images and low (or high) diffusion on diffusion-weighted *FLAIR* (Fluid-Attenuated Inversion Recovery) images. Thus high (or low) cell densities can coexist in poorly perfused volumes, with the creation of perfusion-diffusion mismatches. Regions having poor perfusion and high cell density are of particular clinical interest, because they contain cells which are likely to be resistant to therapy. This highlights the utility of superimposing multiple channels of MR imaging, like *FLAIR, T*2, and contrast enhanced $T1C$ components, in identifying and extracting heterogeneous tumor region(s).

Humans can easily identify the salient (or relevant) parts of an image mainly due to the attention mechanism of the human visual system. "Visual saliency", coined by Ullman and Sha'ashua [35] was extended by Itti et al. [20] towards the development of a computational architecture. Computational models of saliency take images as input and generate a topographical map of how salient or attention grabbing each area of the image can be to a human observer [7]. Such models seem to predict based on certain aspects of human eye movement [14].

Visual saliency can be defined as the outcome of comparing a region with its surrounding, with respect to unpredictability, contrast and rarity [1,25,26,38,43]. The comparison can be done in terms of low level feature similarity. In Ref.[40] authors proposed a novel distance metric learning method termed Semantic Preserving Distance Metric Learning (SP-DML). It encodes the low level feature similarity and semantic similarity in a new unified feature space, from which the similarity/dissimilarity between two image patches can be measured by applying the learned distance metric. In case of the image regions with low visual similarities but high semantic similarities, the traditional similarity measures may not perform well. To deal with this problem many well known approaches have been proposed in the literature based on Hypergraph Learning [39,41].

Saliency detection methods can be broadly classified into (i) biological [20,37], (ii) fully computational [32,42] and (iii) hybrid [4,17]. Algorithms employing the bottom-up strategy detect saliency by using low-level features, like color, intensity, orientation. Those using the top-down strategy include some learning from the training data involving the position or shape of a salient object [34]. It has been observed that often attention is immediately drawn to a salient item, in spite of the existence of many other items (or distracters), without any need to scan the entire image. A visually salient region is typically rare in an image, and contains highly discriminating information. This concept is, therefore, expected to have a major bearing towards the fast identification of an ROI or tumor from a medical image.

Computer Aided Detection (CADe) can be of help to doctors and radiologists in identifying abnormalities, which are comparatively rare, in a medical image. The objective of this research is to improve the present CADe systems by minimizing user interactions, thereby saving precious time of doctors while reducing possibility of human error. Application of visual saliency to medical images is being studied in literature. Jampani et al. [22] investigated the usefulness of three popular computational saliency models, extended from the natural scene framework, to detect abnormalities in chest X-ray and color retinal images. Visual saliency was also applied for automated lesions detection [9,31] from retinal images. Alpert and Kisilev [2] developed a medical saliency model for detecting lesions and microcalcifications in mammograms, MRIs of brain, and stenoses of angiographic images. However sufficient validation study, with respect to ground truth, is not provided. Erihov et al. [12] designed a shape asymmetry-based saliency model for detection of tumors from brain MRI and breast mammograms.

Motivation

Several brain tumor segmentation methods have been developed over the past decade, encompassing supervised as well as semi-supervised techniques [5,19]. While supervised learning involves a separate training phase with a large amount of training data, the semi-supervised methods require user interaction/supervision during segmentation [3]. Cordier et al. [8] developed a multi-channel patch-based segmentation method, which builds a patch database by extracting several patches from the training data for which label maps are available. During testing it searches for similar patches from the training database using some similarity measure. The labelling is performed using leave-one-out scheme. Festa et al. [13] designed a random decision forest, with 50 trees each of depth 25 voxels, for classification-based brain tumor segmentation. Meier et al. [27] used a maximum a posteriori probability (MAP) rule based classification forest for image segmentation. Zhao et al. [44] generated a set of supervoxels which were then labeled using Graph Cuts on a Markov Random Field.

It has been established [30] that semi-automatic segmentation is more robust than manual segmentation, with reference to inter-user variability, while providing comparable output accuracy. Therefore automated algorithms, which are more accurate and require negligible user interaction, are of major interest. Guo et al. [16] employed semi-automatic active contours for segmenting multimodal brain tumors, with the user being required to draw a region of interest (ROI) roughly surrounding the tumor. Grow-Cut [36] is a popular region growing algorithm for semi-supervised segmentation, where the user

inserts seed points on the object and background regions. Based on this user-specified label map, the algorithm iteratively expands the ROI employing the principles of cellular automata.

Contribution

In this paper we propose a novel algorithm, based on the concept of visual saliency, for localizing and segmenting GBM tumor volumes from multi sequence MR images. The saliency detection model is designed to mimic the perception pattern of radiologists. A region is typically considered as visually salient (or attention grabbing) depending on its rarity in the image, thereby signifying the content of some discriminating information (like abnormalities, in the context of medical imaging). Multi-sequence MR images are integrated to generate pseudo-colored MRI for efficiently detecting the whole tumor region. A bottom-up saliency detection strategy, incorporating spatial distance between image patches, is used to highlight the salient region(s) in the pseudo-colored MR image. Next saliency map is used to automatically generate the object and background seed regions. Based on the automatically generated label maps the Grow-Cut method is used to segment the tumor volume (3D) from MR images.

The merits of the proposed saliency based automated tumor detection and segmentation system are outlined below.

- The proposed method is automatic and requires neither a-priori domain knowledge nor training data. Here is no assumption of brain symmetry as in generative models [33].
- Due to the preceding appropriate tumor localization step, the final tumor segmentation can be constrained to the specific suspicious region(s); thereby ruling out any false positives in other (normal) regions of the brain.
- Unlike atlas based approaches [23], the proposed system is highly robust to significant changes and deformations in brain anatomy caused by the presence of abnormality (tumor).
- The semi-supervised Grow-Cut (SGC) segmentation algorithm is automated, thereby eliminating initial user interaction through the generation of multiple initial seed region(s) from the saliency map.
- The automated nature of the system also rules out any inter-observer and inter-scanner error, as is prevalent in clinical setting.

Inter-observer variation is also evaluated for both SGC and our automated algorithm for fast detection and segmentation. The Automated Grow-Cut (AGC) algorithm is found to be more stable w.r.t inter-observer variation, as compared to SGC. All experiments are performed over 30 GBM patient cases from the BRATS database. Furthermore, the segmentation accuracy of AGC is also compared with that of six related state-of-the-art algorithms [8,13,16,27,36,44], as applied to the same database for brain tumor segmentation. In the process AGC is able to eliminate training and/or user interaction, segments in real time, and is more robust to changes in parameters.

The rest of the manuscript is organized as follows. Section 2 presents our algorithm AGC, followed by the experimental results in Section 3. Finally, Section 4 concludes with some discussion on the methodology and its efficacy.

2. Material and methods

2.1. Data used

Brain tumor image data used in this work was obtained from the MICCAI 2013 Challenge on Multimodal Brain Tumor Segmentation[1] organized by B. Menze, A. Jakab, S. Bauer, M. Reyes, M. Prastawa, and K. Van Leemput. There are 30 glioma cases, of which 20 are of High-grade (HG) and 10 of Low-grade(LG), with four MR sequences *T*1, *T*1*C, T*2, and *FLAIR* being available for each patient. The challenge database contains fully anonymized images collected from ETH Zurich, University of Bern, University of Debrecen, and University of Utah. All images are linearly co-registered and skull stripped. Since all data on human subjects is publicly available and de-identified, therefore no Institutional Review Board approval was required [24,28].

2.2. Methodology

We developed a novel saliency based tumor detection model for brain MR images of glioma, using the three MRI sequences *viz. FLAIR, T*2 and *T*1*C* for mapping to a pseudo-color space. The concept of visual saliency is employed to enable the algorithm quickly focus on the ROI. The pseudo-coloring strategy for MR images efficiently generates the saliency map for highlighting the location of the tumor. The object map is next computed from the saliency map, followed by its segmentation using state-of-the-art region growing based method.

2.2.1. Pseudo-coloring

Digital color images are often constructed from three stacked color channels *viz.* red, green and blue (*RGB*). These can be decomposed to three gray scale images, in six ways, and recomposed back to the *RGB* image. For example, let us consider three gray-scale images *A, B, C*, and let *A* be assigned to Red, *B* to Green, and *C* to Blue channel. Then the six combinations are *ABC, ACB, BAC, BCA, CAB, CBA*.
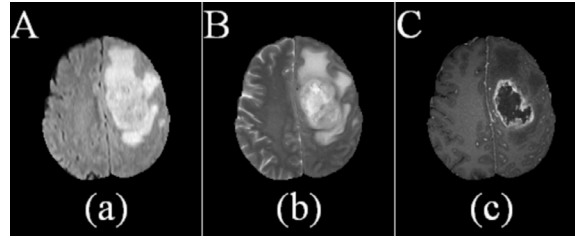

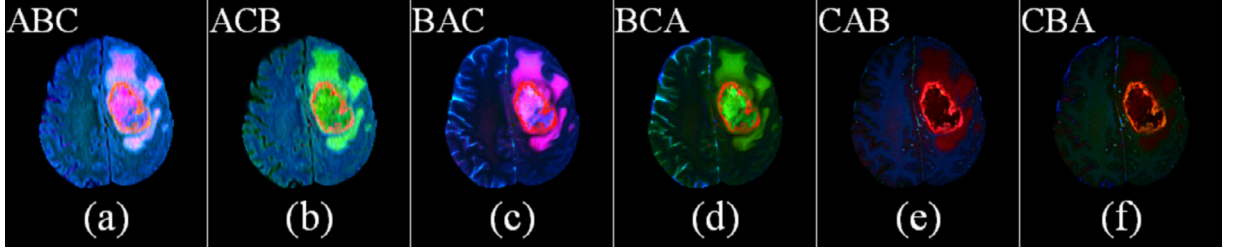Fig. 1. Sample MRI sequences. (a) FLAIR, (b) T2, and (c) T1C.

Fig. 2. Six corresponding pseudo-colored ($L^*a^*b^*$) converted brain MR image sequences. (For interpretation of the references to colour in this figure legend, the reader is referred to the web version of this article.)

We assign the three MR sequences (*FLAIR, T2, T1C*) to *RGB* for generating a "pseudo-color" MR image. This yields a 48 bit MR image containing more information than a single-channel gray-scale image. Thereby a color MR image is capable of detecting and displaying the whole tumor region as the ROI from such pseudo-color projections.

Since our saliency detection algorithm depends on the center-surround difference of a region with its neighbors, based on the pixel color values, a perceptually uniform color space that decorrelates luminance from chrominance information becomes desirable. Therefore we choose to transform the RGB space to the International Commission on Illumination (CIE)-recommended $CIE - L^*a^*b^*$ domain, with the Euclidean distance ΔE_{76} representing the color difference. Here $\Delta E_{76} = \|V_i - V_j\|$, with $\|.\|$ expressing the L_2-norm [21] and $V_i = L_i^*, a_i^*, b_i^*$, $V_j = L_j^*, a_j^*, b_j^*$. Converting an *RGB* image to $L^*a^*b^*$ results in the separation of luminosity (layer L^*) and chromaticity (layer a^*, which indicates the position of the color along the red-green axis, and layer b^*, which represents the position of the color along the blue-yellow axis). Fig. 1 shows sample MRI sequences and Fig. 2 illustrates the corresponding $L^*a^*b^*$ converted MR images.

It is visually obvious from the figure that in the first two sequence sets, *ABC* and *ACB*, only the tumor and edema regions get highlighted while all other regions are suppressed. The next two sequence sets *BAC* and *BCA* serve to additionally illuminate the *CSF* region due to its hyper-intense appearance in *T*2. The last pair of sequence sets *CAB* and *CBA* cause the edema to be suppressed due to its hypo-intense appearance in *T1C*, with the discrimination between the object and background being minimally visible. Therefore we can use either of the first two sequence sets *ABC* or *ACB* for the saliency detection procedure, because here the ROI gets enhanced while suppressing the less relevant regions of the brain. In this study we choose the sequence set *ABC* for subsequent saliency detection.

Thus the pseudo-coloring scheme first creates a pseudo-colored *RGB* image from the *FLAIR, T2, T1C* MR image, and then transform from *RGB* color space to *CIE–L*a*b** color space to enhance local contrast. This is followed by the generation of local and global contrast-based saliency map for detecting the whole tumor region, as described below.

2.2.2. Tumor location with saliency

The salient region of an image is defined by one (or more) very important piece(s) of the composition, which make it stand out from its surroundings. An $L^*a^*b^*$ image (of size $M \times N$) is first transformed to a square image of size $w \times w$. Since the database can contain images of different sizes, these need to be converted to one uniform size (preferably a squared one, here $w = 256$). Then it is decomposed into several non-overlapping blocks R_i (or patches) of size $k \times k$ pixels (where w is a multiple of k), with each being represented by its mean $L^*a^*b^*$ values. The number of patches ($w/k \times w/k$) correspond to the number of pixels in the saliency map. Let the ith patch of the image $I(R_i)$, $1 \leq i \leq (w/k \times w/k)$, be represented by its mean $L^*a^*b^*$ color values as

$$R_i^{\bar{L^*}} = \frac{\sum I(R_i^{L^*})}{k \times k}, \bar{R}_i^{a^*} = \frac{\sum I(R_i^{a^*})}{k \times k}, \bar{R}_i^{b^*} = \frac{\sum I(R_i^{b^*})}{k \times k}. \tag{1}$$

Next the saliency of each patch is calculated with respect to all other patches in the image. Color is considered as the most important feature in the bottom-up approach, with the simple color difference between regions providing an efficient way to highlight the salient region(s) with respect to the non-salient patches. The color difference between a pair of patches is defined as the Euclidean distance between the corresponding mean color values of $L^*a^*b^*$. Therefore, for patch R_i, the
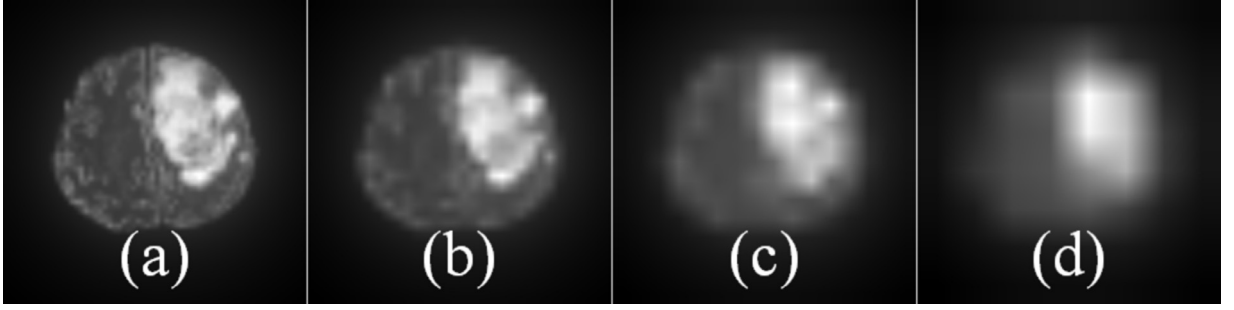
Fig. 3. Saliency map of pseudo-colored MR image of the whole tumor region of Fig. 2 (a) at different scales. Patch sizes of (a) 4×4, (b) 8×8, (c) 16×16, and (d) 32×32.

saliency $S(R_i)$ is calculated as the sum of the color difference between $R_i^{\bar{L}*}$, $R_i^{\bar{a}*}$, $R_i^{\bar{b}*}$ and $R_j^{\bar{L}*}$, $R_j^{\bar{a}*}$, $R_j^{\bar{b}*}$ (Eq. (1)), $\forall\ j \neq i$. This constitutes the numerator on the r.h.s. of Eq. (2). When the sum of color difference of a patch with respect to the remaining patches in the image is large, then it is considered to be salient.

$$S(R_i) = \sum_{j \neq i} \frac{1}{1 + d(R_i, R_j)} \times \sqrt{(R_i^{\bar{L}*} - R_j^{\bar{L}*})^2 + (R_i^{\bar{a}*} - R_j^{\bar{a}*})^2 + (R_i^{\bar{b}*} - R_j^{\bar{b}*})^2}$$

$$\forall i, j \in \{1, \ldots, (w/k \times w/k)\}. \tag{2}$$

While most salient patches are typically concentrated around spatially adjacent areas, the other patches (which are normally not salient) may be distributed anywhere over the entire image. If a region is salient then the probability for its surrounding regions to be also salient is larger, while the probability of those regions located farther away being salient becomes smaller. So the influence of adjacent regions can be considered to be more important when computing the saliency of a region. Therefore we incorporate the spatial distance between patches as another important factor while computing image saliency. In the process, we consider (i) the difference of the mean $L^*a^*b^*$ color values between any two blocks, and (ii) the spatial distance between them. This is represented by the denominator on the r.h.s. of Eq. (2). Here $d(R_i, R_j) = \sqrt{(\bar{x}_{R_i} - \bar{x}_{R_j})^2 + (\bar{y}_{R_i} - \bar{y}_{R_j})^2}$, where $d(R_i, R_j)$ is the spatial distance between the patches R_i and R_j of the image, and $(\bar{x}_{R_i}, \bar{y}_{R_i})$ refers to the mean spatial coordinates of R_i.

When an observer views a far-off scene, the focus lies on the entire salient region(s). Again when the same scene is viewed at a closer range, the observer tends to pay greater attention to the details within the salient region [11,20]. We adopt this property of the human visual attention mechanism into our model through the evaluation of saliency maps at multiple scales. We are able to clearly highlight the salient object, at a higher resolution, by partitioning the image into smaller sized patches.

A saliency map can be considered to be a probability map, with the intensity of a pixel indicating its chance of belonging to the tumor region in the original image. While a saliency value 0 (pure black, when considered as a gray scale image) indicates least importance, an intensity of 1 (pure white) corresponds to highest importance. Although the saliency map for a larger patch can help in accurately locating a salient object, its resultant blurring causes disappearance of most details.

Saliency maps, depicting the saliency strength at every pixel over different scales, involving varying sizes of the patches (with $k = 4$, 8, 16, 32, of sizes 4×4, 8×8, 16×16 and 32×32) are provided in Fig. 3 (post-rescaling to their original sizes). These images correspond to the tumor and edema regions of Fig. 2(a). We observe that as the contour of the ROI gets gradually blurred, with increasing patch size k, the position of the salient region becomes clearer. Here the block size k relates to the resolution of the saliency map.

Re-scaling is performed to bring back the saliency maps to the original image size ($M \times N$) using Bilinear interpolation [11]. Let $\hat{S}^k$ denote the interpolated image at its original size, as generated from the saliency map S^k at scale k. Since the properties of a region depend on the pixels within it, saliency prediction is governed by both its size and scale. Thus our algorithm is simultaneously employed over multiple scales, analogous to [11], for capturing the salient region(s) in the *MR* image at different levels of resolution. Those region(s) consistently highlighted over different resolutions are deemed to be the ones most likely to be salient. Therefore we superimpose these saliency maps, corresponding to the different scales, for computing the final map. For example, the integrated map over the four scales (of Fig. 3) contains all important information and is depicted in Fig. 4(a). The final saliency map is now computed as

$$S = \sum_{k=4,8,16,32} r^k \times \hat{S}^k, \tag{3}$$

where r^k is the weight corresponding to the saliency map at size k. In the present study we have chosen $r^k = 1/4$, $\forall\ k$. Finally a 25×25 mean filter is applied to smoothen the saliency map S, in order to help focus on the core region within the actual ROI in the resized image. This is depicted in Fig. 4(b), and acts as the reference map for subsequent segmentation.
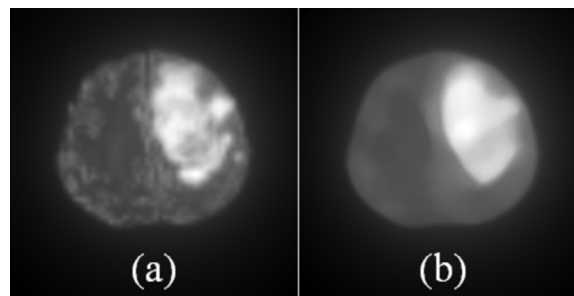
Fig. 4. Final saliency map. (a) Superimposed saliency map corresponding to Fig. 3, and (b) its final smoothened version.
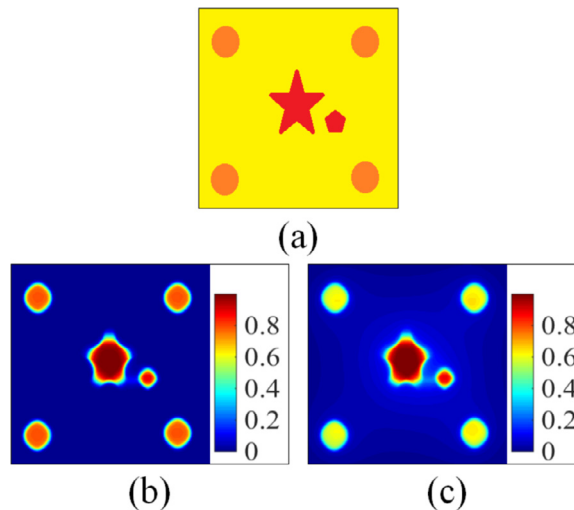

Fig. 5. Effect of incorporating spatial distance for saliency map. (a) Input image. Heat map of final saliency map, (b) without incorporating spatial distance, and (c) incorporating spatial distance. (For interpretation of the references to colour in this figure legend, the reader is referred to the web version of this article.)

The underlying assumption about spatial coincidence identifies a region as salient only if it is found to be consistently salient over multiple scales.

Let us illustrate the usefulness of incorporating spatial distance through a simulated illustration. Fig. 5(b) shows the saliency maps, corresponding to the image of Fig. 5(a), without considering spatial distance between the patches. Fig. 5(c), on the other hand, demonstrates the effect of incorporating the spatial distance component between the patches. The simulated image contains six objects, consisting of four circles, one star, and one pentagon. A significant color difference between all objects and the background is observable in the image. However the star and the pentagon are seen to attract our attention, possibly due to their position, size, uniqueness with respect to color, and their exclusiveness. Fig. 5(c) demonstrates an accurate detection (lower false positive) of the salient region (higher value on the heat map), as compared to Fig. 5(b) in the absence of the spatial distance component in Eq. (2). Analogously the less salient circles get mapped to a lower value on the heat map, thereby distinguishing them from the star and pentagon.

Although MR images of brain contain several tissues other than tumor(s), with significant contrast difference w.r.t. the background region, these are not visually salient because they are neither unique nor exclusive as compared to the latter. Since there exists significant contrast difference between such other regions of the image, therefore not incorporating the spatial distance component results in these regions acquiring reasonably high saliency scores (analogous to Fig. 5(b), where the circles are also considered as salient objects, unlike Fig. 5(c)). Another important observation is that the whole tumor region may not be connected but coexist in spatially adjacent locations. This phenomenon is mimicked in the simulated image by the small pentagon adjacent to the salient star, which is collectively considered to be the salient tumor region. It is evident from the figures that incorporation of spatial distance helps to efficiently detect the most salient object along with all adjacent, small, visually striking objects.

2.2.3. Modification for 3D saliency map

Generation of saliency maps is next extended over the 3D stack of such 2D MR image slices, each encompassing the three MR sequences. However for the slices having too small foreground, as compared to the background, our saliency detection
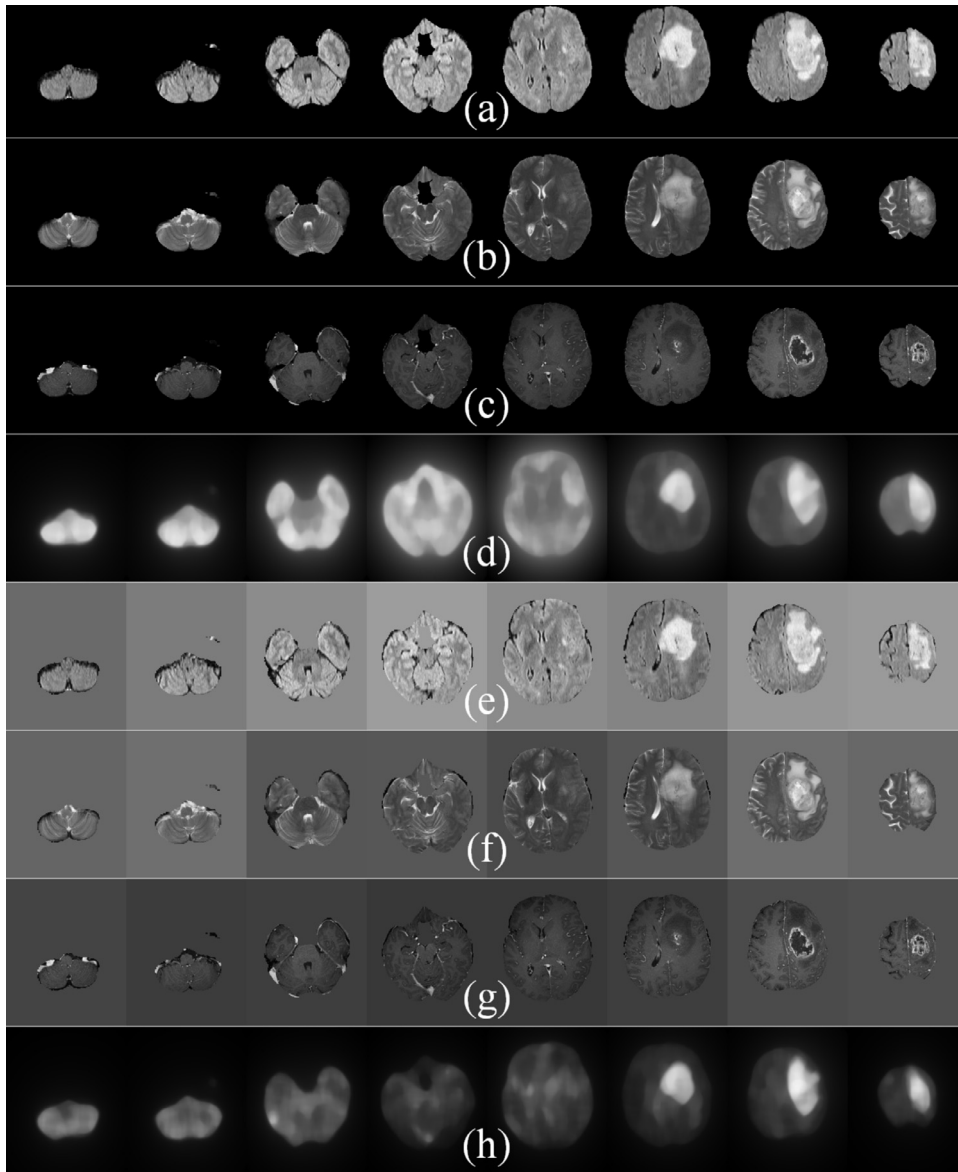
Fig. 6. 2D saliency maps corresponding to the 2D MR slices of a High-grade glioma patient from BRATS data base (Patient ID = brats_2013_pat0011_1). MR slice numbers: 13, 19, 35, 46, 67, 81, 100, 121 (left to right) by (a) *FLAIR*, (b) *T2*, and (c) *T1C* sequences. (d) Saliency maps generated from the original slices. Modified MR slices, with mean intensity values replacing background pixels, for (e) *FLAIR*, (f) *T2*, and (g) *T1C* sequences. (h) Saliency maps from the modified MR image slices, where ROI is clearly visible/salient in last three slices.

algorithm can produce false positive results. This is evident from MR images constituting the starting and ending slices of the 3D stack of brain images, as depicted in Fig. 6(a)–(d). This is because Eq. (2) computes saliency based on the mean color difference between patches, thereby highlighting the small foreground regions in such 2D slices (Fig. 6(d)). In order to circumvent this problem all background pixels, in each of the three sequences, are now replaced by their mean image intensity values in Fig. 6(e)–(g). In this modified framework the saliency detection algorithm effectively ignores such skewed situations, as evident from Fig. 6(h). The ROI is seen to be accurately detected in the last three columns of Fig. 6(h).

2.2.4. Object and label map

According to the object-based attention theory [6], human visual processing starts with the segmentation of an image into connected regions, which are also termed as proto-objects or *pre-attentive objects*. Each proto-object is then assigned an importance value, which is called its saliency score. Then the attention or focus reaches the most salient proto-object in the scene or image. In the present scenario, after generating the saliency map (consisting of the saliency value of each voxel),
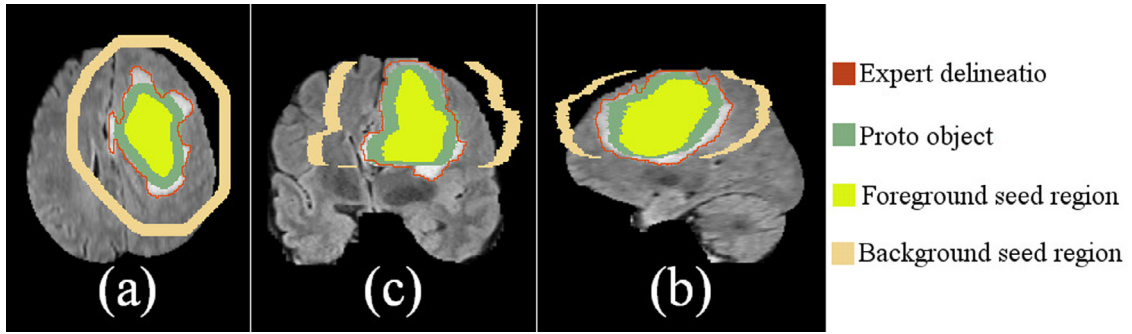
Fig. 7. Label map generation from the proto-object. Proto-object (green), marked foreground (green-yellow) and background (gold) are shown for (a) axial, (b) sagittal, and (c) coronal views. (For interpretation of the references to colour in this figure legend, the reader is referred to the web version of this article.)

the most salient (or main) 3D proto-object is extracted by segmentation using an adaptive threshold (Fig. 7) selected as the mean of the local gray scale distribution.

The main proto-object is then used for generating the foreground and background seed regions on the MR images. The foreground seed region is computed by shrinking the size of the proto-object using morphological erosion operation, with a circular structuring element. This is needed to provide tolerance for the positioning of the actual boundary of the proto-object, by reducing the number of false positives, as demonstrated in Fig. 7. Next the proto-object is enlarged by applying the morphological dilation operation, with a circular structuring element using a pair of radii $r_1 < r_2$. Let dilation using r_1 and r_2 result in enlarged proto-objects 'α' and 'β' respectively, as shown in Fig. 7. The pixels within the region $\beta - \alpha$ are selected as the background pixels, as highlighted in Fig. 7. Now the marked foreground and background pixels serve as the 3D label map of the image, for subsequent region growing based segmentation.

2.2.5. Automated segmentation

Finally the 3D label map is used for automated segmentation of the tumor region. Any state-of-the-art region growing based method may be employed. We choose to explore the *Grow-Cut (GC)* algorithm [36] which is reported in Ref.[10] to be good for tumor delineation in medical images. Grow-Cut typically requires the user to insert seed points, both on the object and the background regions (constituting the user-specified label map), based on which the algorithm iteratively expands the ROI following the principles of cellular automata (CA). Our algorithm, on the other hand, automatically generates the 3D label map based on saliency (as described in Section 2.2.4) for subsequent Grow-Cut segmentation. Since the label map entails no user interaction, it is termed the unsupervised or automated version of Grow-Cut (AGC).

Algorithm AGC incorporates a CA based framework, with each pixel $p \in P$ of the input image being considered as a cell. A cellular automaton is defined using a triple (S, N, δ), where S is the state, N is the neighborhood and δ is the state transition function (rule). Here the state of each cell is given by a 3-tuple (l, θ, I), where l is the label, $\theta \in [0, 1]$ is its strength and I is the pixel intensity. The 3D label map produced from the saliency map (Section 2.2.4) is used as the initial label map. The strength of all foreground pixels are assigned to cell strength 1, while the background pixels are set to 0. This defines the initial state of the cellular automaton. At iteration $t + 1$ cell label l_p^{t+1} and strength θ_p^{t+1} are updated by Algorithm 1.

Algorithm 1 AGC state update.

1: **procedure** UPDATE(l^t, θ^t)
2:     **for** $p \in P$ **do**   ▷ For all pixels in the image copy previous state
3:         $l_p^{t+1} = l_p^t$;   ▷ $labels_{new}(p) = labels(p)$
4:         $\theta_p^{t+1} = \theta_p^t$;   ▷ $strength_{new}(p) = strength(p)$
5:     **end for**
6:     **for** $q \in N(p)$ **do**   ▷ Neighbors try to attack current cell
7:         **if** $g(||I_p - I_q||_2).\theta_q^t > \theta_p^t$ **then**
                                         ▷ $attack\_force(p, q) \times strength(q) > strength(p)$
8:             $l_p^{t+1} = l_q^t$;   ▷ $labels_{new}(p) = labels(q)$
9:             $\theta_p^{t+1} = g(||I_p - I_q||).\theta_q^t$;
                                         ▷ $strength_{new}(p) = attack\_force(p, q) \times strength(q)$
10:         **end if**
11:     **end for**
12: **end procedure**

Here g is a monotonically decreasing function, bounded by [0,1], and is defined as $g(x) = 1 - \frac{x}{\max(I)}$.
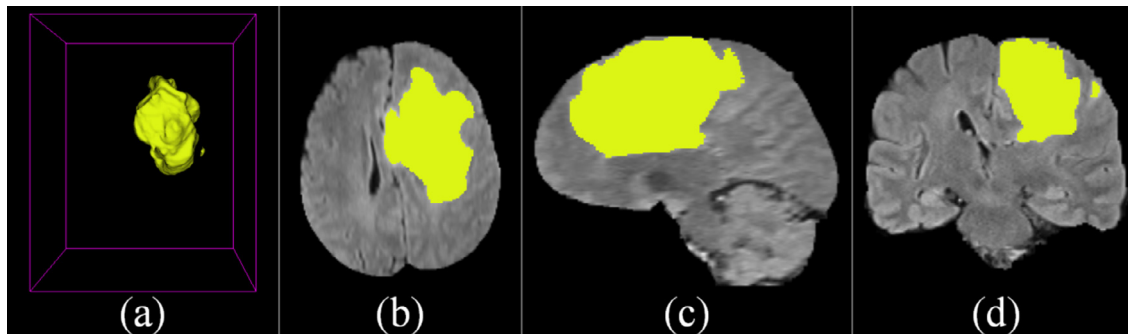
Fig. 8. Final segmented tumour (green-yellow), in AGC, for (a) three dimensional, (b) axial, (c) sagittal, and (d) coronal views. (For interpretation of the references to colour in this figure legend, the reader is referred to the web version of this article.)

The software system for algorithm AGC requires the user to initialize the foreground and background regions by marking the areas inside and outside the tumour region with few seed pixels. Our saliency based algorithm, on the other hand, automatically generates the initial label map (foreground and background regions) as depicted in Fig. 7. This serves as the initialization phase for AGC, with the axial, sagittal, and coronal view illustrated in Fig. 7. Next Algorithm 1 enables automatic competitive region-growing for segmentation of the ROI into foreground and background areas. The final segmented tumour region is displayed in Fig. 8 for the sample example under consideration.

3. Experimental results

Clinical significance and reliability of the saliency based model was evaluated in terms of its accuracy in automatically locating the initial tumor region for subsequent unsupervised segmentation from 3D MR images using region growing techniques (like Grow-Cut).

Different binary masks are generated for the salient object by thresholding the saliency map, over varying thresholds (ranging from 0 to 1). These were compared with the ground truth, based on different metrics like precision-recall, receiver operator characteristic (*ROC*) curves and the area under the *ROC* curve (*AUC*) statistics, as used in literature. The resulting segmentation output was also evaluated, both in terms of the accuracy as well as repeatability (or reusability) of results.

3.1. Evaluation of saliency map

The performance of the algorithm was evaluated by computing the Precision-Recall, Receiver Operator Characteristic (*ROC*) [true positive rate (*TPR*) vs. false positive rate (*FPR*)] curves, and the area under the *ROC* curve (*AUC*). Each generated saliency map was considered to be a binary classifier, distinguishing between positive and negative samples, over different thresholds in the range [0, 1]. The precision-recall and *ROC* curves, computed by averaging over all images for each data group (HG and LG), are shown in Fig. 9. The 3D saliency maps of six patients is illustrated in Fig. 10.

Precision corresponds to the percentage of salient pixels correctly assigned, while recall represents the fraction of detected salient pixels with reference to the ground truth. High recall can be achieved at the expense of reducing the precision, and vice-versa. Therefore it is important to evaluate both measures together. *TPR* is the proportion of saliency map values above the threshold at actual locations, while *FPR* is the proportion of those values above the threshold at non-existent pixels (corresponding to non-tumorous regions from the ground truth).

The accuracy of the model is measured by the area under the *ROC* curve, which was found to be **0.98 ± 0.015** in the high-grade cases and **0.99 ± 0.004** in the low-grade cases. Such high *AUC* scores allow us to infer that the proposed saliency model can robustly and accurately detect the tumor regions for both high-grade as well as low-grade GBM samples.

3.2. Evaluation of automated segmentation

The utility of our algorithm lies in using saliency maps for automating the Grow-Cut segmentation. As indicated earlier, by circumventing the issue of user interaction during seed point insertion (for generating the label map) we are able to eliminate any subjective bias for the accuracy of the subsequent region growing segmentation used. Moreover, unlike the automated procedure observed in our algorithm AGC, a manual insertion of seed points is done in Grow-Cut with reference to the ground truth. Ideally the misclassification error for the label map, with respect to corresponding ground truth, should be zero; implying correct placement of the object and background seeds. In our case the automatically generated 3D label map (based on the saliency map) is always found to match with the corresponding ground truth for all 30 patients – irrespective of tumor type (HG or LG), size, shape and/or location. This can be validated from the segmentation scores of the proposed automated Grow-Cut (AGC), as compared to that of the semi-automated Grow-Cut (SGC) initialized by the manually generated label maps.
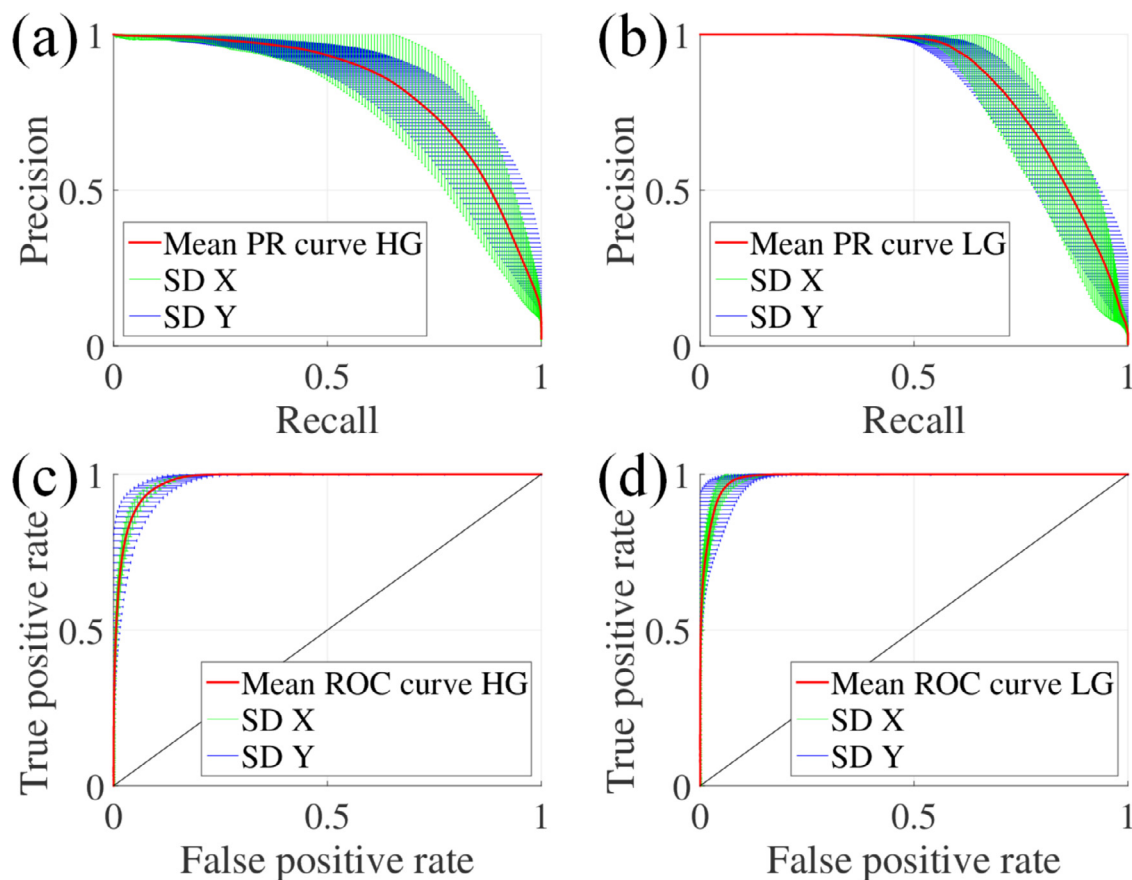
Fig. 9. Precision-Recall and ROC curves. Precision-recall curves for (a) HG, (b) LG, and ROC curves for (c) HG, (d) LG, over the saliency maps for different thresholds. Blue and green error bars represent the standard deviation along abscissa and ordinate, respectively. (For interpretation of the references to colour in this figure legend, the reader is referred to the web version of this article.)
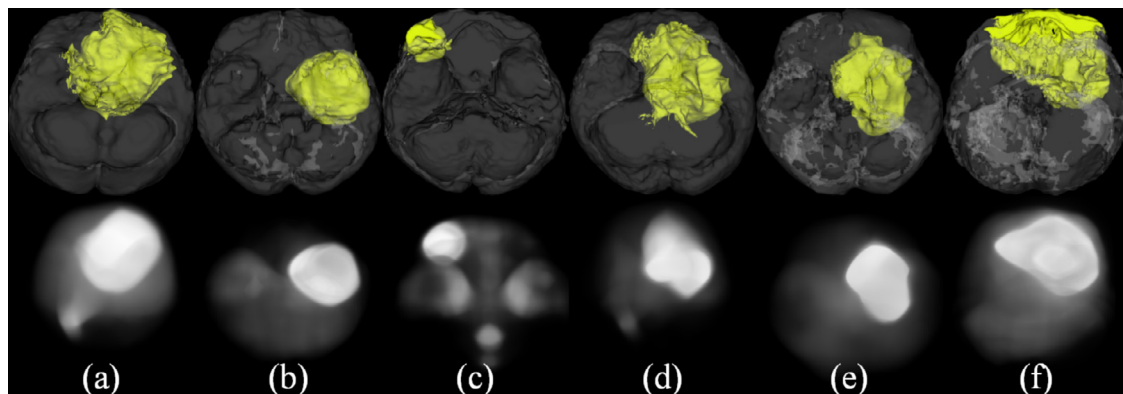

Fig. 10. Ground truth and corresponding 3D saliency maps of six patients from the BRATS database. (For interpretation of the references to colour in this figure legend, the reader is referred to the web version of this article.)

Results are provided over sample patients from the BRATS database, with 20 having HG and 10 suffering with LG GBM. Let $Y \in \{0, 1\}$ represent the segmented image, and $T \in \{0, 1\}$ correspond to the expert-level consensus truth image.

3.2.1. Accuracy metrics

The segmentation accuracy is measured (w.r.t. ground truth volume) in terms of (i) overlap-based metric called the Dice coefficient (DICE), also known as the overlap index, (ii) volume-based metric called volumetric similarity (VSMTY), and (iii) spatial distance-based metric termed Average Hausdorff Distance (AVGHD).

(i) Dice coefficient:

$$DICE(Y, T) = \frac{|Y_1 \wedge T_1|}{(|Y_1| + |T_1|)/2},$$
(4)

where $\wedge$ is the logical AND operator, $|.|$ represents the cardinality of the set in terms of voxels, and Y_1, T_1 correspond to the set of voxels where $Y = 1$ and $T = 1$, respectively. *DICE* measures the voxel-wise overlap of the segmented region(s) with the ground truth.

(ii) Volumetric similarity:

VSMTY is '1' when the cardinalities of Y_1 and T_1 are equal, and zero when one of them is empty. We compute

$$VSMTY(Y, T) = 1 - \frac{||Y_1| - |T_1||}{|Y_1| + |T_1|},$$
(5)

which compares only the corresponding volumes (without reference to the actual voxels involved); thereby implicitly assuming that the segmented regions are optimally aligned with the ground truth. As a result *VSMTY* can have its maximum value (one) even when the overlap is zero. However when the volume of the segmented region is of greater importance, as compared to its boundary and/or alignment, then *VSMTY* is evaluated.

(iii) Average Hausdorff Distance:

Metrics sensitive to point positions, like *AVGHD*, are able to evaluate segments with reference to the correctness of their contours (or boundaries). AVGHD measures the Hausdorff distance between all pairs of voxels, and is expressed as

$$AVGHD(Y, T) = \max\{d(Y, T), d(T, Y)\},$$
(6)

where $d(Y, T)$ is the directed average Hausdorff distance $d(Y, T) = \frac{1}{N} \sum_{y \in Y_1} \min_{t \in T_1} ||y - t||$, and $||.||$ represents the Euclidean distance.

It is obvious that a higher similarity by *DICE* and *VSMTY*, and a lower distance by *AVGHD*, are indicative of better segmentation accuracy w.r.t. the ground truth.

3.2.2. Reliability and robustness

Evaluation of segmentation variability provides a judgement on the repeatability of the algorithm as well as the acceptable range of error. The coefficient of variation *CV*(%) is a way of measuring the inter-observer variability error. It is computed as

$$CV = 100 \times (SD_{volume} / Mean_{volume}),$$
(7)

where $Mean_{volume}$ represents the mean tumor volume in mm^3 over the observers, and SD_{volume} represents the corresponding standard deviation. Here *CV* does not measure the correctness of the segmentation, but it only evaluates the change in the volume of objects between segmentation operations performed by different observers.

The Pearson correlation coefficient ρ is used to evaluate the correlation between the whole tumor volume and the three accuracy metric scores *DICE, VSMTY*, and *AVGHD*. It is defined as

$$\rho_{(\text{tumor size, accuracy metric})} = \frac{cov(\text{tumor size, accuracy metric})}{\sigma_{\text{tumor size}} \; \sigma_{\text{accuracy metric}}},$$
(8)

where $-1 \le \rho \le 1$, *cov* is the covariance and σ represents the standard deviation. This helps estimate the robustness of the proposed method, which is intended to produce stable segmentation accuracy despite variations in tumor size.

3.2.3. Computational complexity

Computational complexity of the proposed method is an aggregation of the complexity of its two parts, viz. saliency detection and the segmentation. The computational time complexity of the saliency detection part can be asymptotically represented as (assuming $M > N$),

$$T = 155 \times \left[\sum_{k=4,8,16,32} (M/k)^2 \times \{(M/k)^2 - 1\} + C \right]$$

$$\simeq \mathcal{O}(M^4)$$
(9)

where C is a constant, and the computational time complexity of the segmentation method is also $\mathcal{O}(M^4)$. So, the computational complexity of the proposed method is $\mathcal{O}(M^4)$.

Since, the computational cost of our algorithm is very low, therefore it can be easily implemented in real time or inter-operative environment in a parallel realization.

3.2.4. Implementation

Three independent observers, having adequate knowledge in semi-automatic segmentation and blinded to each other, were required to individually segment the whole tumor region(s) for this purpose. Ground truth generation protocol for the BRATS database uses the *FLAIR* and *T*2 MR sequences for the process [28]. In order to maintain parity we employed only these two sequences during segmentation by SGC and AGC. While in SGC each observer manually selects a seed ROI randomly from the corresponding ground truth image, in case of AGC a label map is automatically generated from the saliency map.

The three observers performed twelve segmentation operations (on each of the 20 HG and 10 LG patients), six each by SGC and AGC, such that there were three outputs in each case from MR sequences *FLAIR* and *T*2 respectively. The final segmentation output of the GC method depends on the initial label map. Therefore, in case of the AGC no inter-observer variability was observed as the label maps were generated automatically. On the other hand, in case of SGC a significant amount of inter-observer variability was present due to the manual generation of label maps by each observers. The experimental results for inter-observer variability, related to both methods, are given in Section 3.2.5.

All the segmented volumes were compared with the corresponding ground-truth volume, manually delineated by expert radiologists, with respect to the three metrics *DICE, VSMTY*, and *AVGHD* of Eqs. (4)–(6). Then two average *DICE, VSMTY*, and *AVGHD* scores were computed from the segmentation scores of the three observers, for both sequences.

3.2.5. Results

Here we present the results evaluating the performance of our algorithm, both in terms of accuracy and reliability of the segmentation.

(i) Accuracy

The box-and-whisker plots in Fig. 11 report the minimum, lower quartile, median, upper quartile and maximum for each metric (*DICE, VSMTY*, and *AVGHD*) of the three observers, for 20 HG and 10 LG patients from each of the two groups, using SGC and AGC. Points which fall outside 1.5 times the interquartile range are considered as outliers. The proposed algorithm AGC, initiated by the label map generated through saliency, always produces significantly improved segmentation accuracy as compared to SGC (initiated from a manually generated label map). This is evident from Fig. 11 and Table 1, with the improvements (as compared to SGC) found to be statistically significant at the 0.05 level using independent samples *t*-test and the *p*-values being reported for all cases in Table 1.

The overall mean and standard deviation for *DICE, VSMTY*, and *AVGHD* scores over the 20 HG cases were 0.86 ± 0.06, 0.93 ± 0.04, 0.39 ± 0.40, respectively, by AGC using *FLAIR*. In case of SGC these scores were 0.78 ± 0.09, 0.86 ± 0.12, 1.22 ± 0.98, respectively, using FLAIR. These are illustrated in Fig. 11(a), (c), (e) and the first row of Table 1, with the best scores highlighted in each case. Analogous results for the ten LG glioma cases were 0.85 ± 0.07, 0.94 ± 0.06, and 0.33 ± 0.26, corresponding to *DICE, VSMTY, AVGHD*, with AGC using *FLAIR*. For SGC and LG glioma, on the other hand, MR sequence *T*2 provided better performance at 0.73 ± 0.11, 0.86 ± 0.12, 1.29 ± 1.21, corresponding to *DICE, VSMTY, AVGHD*, respectively. This is depicted in Fig. 11(b), (d), (f) and the second row of Table 1. Fig. 11 demonstrates that AGC has stable quantitative performance over different observers. On the other hand, a huge inter-observer variability is obtained in case of SGC for all three metrics. Experimental results illustrate that the FLAIR sequence produces superior segmentation accuracy as compared to T2. This is validated by the observation that FLAIR appears to be the best in determining the margins of glioma, perhaps due to the absence of partial volume effect caused by nullified CSF.

Table 2 provides a comparative study of five other state-of-the-art segmentation algorithms developed for brain tumor segmentation, along with SGC and AGC, as applied on the BRATS database [28] and measuring accuracy in terms of *DICE* as well as average time of computation (in min) as evaluated on CPU-based and cluster architectures. It is observed that AGC performs the best on both counts. It is also to be noted that all supervised algorithms consume additional training and preprocessing time.

(ii) Reliability and Robustness

Inter-observer variability *CV*(%) was observed to be nil in case of AGC; while for SGC the corresponding values were $2.62\% - 10.51\%$ and $3.5\% - 14.42\%$. Fig. 12 shows the inter- observer variability achieved by the SGC and AGC algorithms, with the corresponding horizontal lines indicating the mean value over 20 HG and 10 LG glioma samples.

It is observed from Fig. 13 that all three metrics, *DICE, VSMTY* and *AVGHD*, present weak correlation ρ with respect to total tumor volume over both MR sequences. This implies that a variation in tumor size does not significantly influence the segmentation accuracy of our algorithm, in other words, it is robust to the size of the tumor.
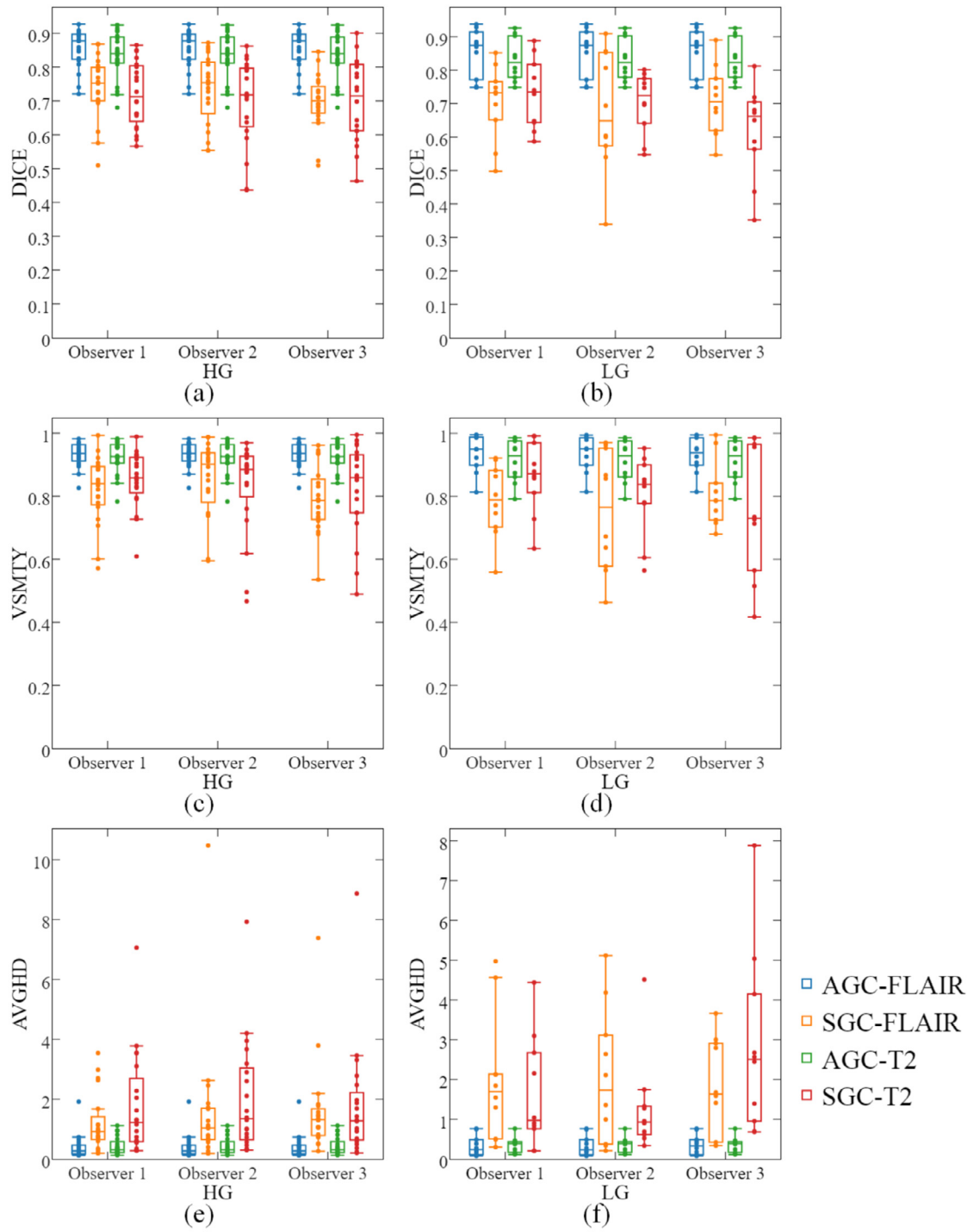
Fig. 11. Box-and-whisker plot of segmentation accuracy of three observers with *DICE, VSMTY,* and *AVGHD* for *FLAIR* and *T*2 MR sequences, using AGC and SGC. The central line in each box indicates the median. Metrics *DICE* for (a) HG, (b) LG cases; *VSMTY* for (c) HG, (d) LG cases, and *AVGHD* for (e) HG, (f) LG cases. (For interpretation of the references to colour in this figure legend, the reader is referred to the web version of this article.)
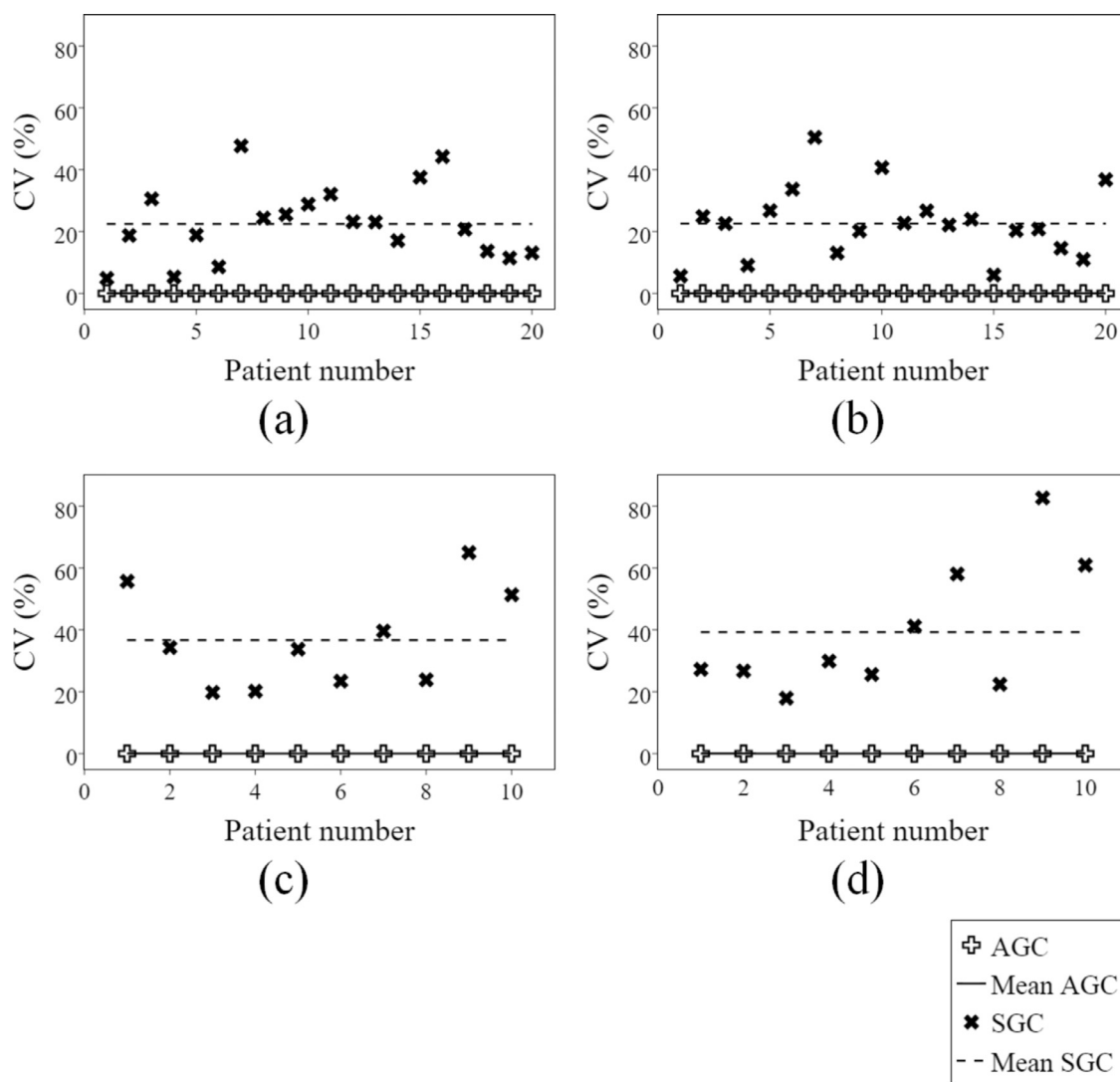
Fig. 12. Comparative inter-observer variability CV for AGC and SGC, over HG using (a) FLAIR, (b) T2 MR sequences, and over LG using (c) FLAIR, (d) T2 sequences.
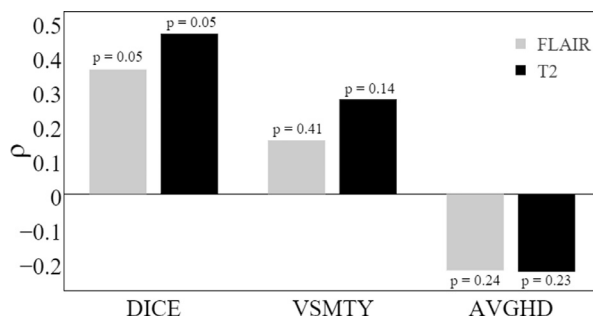

Fig. 13. Pearson correlation coefficient ρ of the three metrics (*DICE, VSMTY* and *AVGHD*) with total tumor volume, over both MR sequences *T*2 and *FLAIR*. The *p*-values indicate the significance of the correlation.

Table 1

Comparative study of segmentation accuracy for three observers, using AGC and SGC algorithms for glioma patients (single-sided paired *t*-test, with * and ** corresponding to $p < 0.05$, and $p < 0.01$, respectively).

Grade(#)	Observer	Metric	Sequence	AGC	SGC	*p*-value
HG (20)	1	DICE	FLAIR	**0.86 ± 0.06**	0.78 ± 0.09	**
			T2	0.83 ± 0.07	0.72 ± 0.09	**
		VSMTY	FLAIR	**0.93 ± 0.04**	0.82 ± 0.11	**
			T2	0.92 ± 0.05	0.85 ± 0.10	**
		AVGHD	FLAIR	**0.39 ± 0.40**	1.22 ± 0.98	**
			T2	0.43 ± 0.30	1.78 ± 1.70	**
	2	DICE	FLAIR	**0.86 ± 0.06**	0.73 ± 0.10	**
			T2	0.83 ± 0.07	0.70 ± 0.13	**
		VSMTY	FLAIR	**0.93 ± 0.04**	0.86 ± 0.012	*
			T2	0.92 ± 0.05	0.83 ± 0.15	*
		AVGHD	FLAIR	**0.39 ± 0.40**	1.57 ± 2.20	*
			T2	0.43 ± 0.30	2.02 ± 1.90	**
	3	DICE	FLAIR	**0.86 ± 0.06**	0.69 ± 0.08	**
			T2	0.83 ± 0.07	0.70 ± 0.12	**
		VSMTY	FLAIR	**0.93 ± 0.04**	0.79 ± 0.10	**
			T2	0.92 ± 0.05	0.82 ± 0.14	*
		AVGHD	FLAIR	**0.39 ± 0.40**	1.61 ± 1.56	**
			T2	0.43 ± 0.30	1.79 ± 1.93	**
LG (10)	1	DICE	FLAIR	**0.85 ± 0.07**	0.70 ± 0.11	**
			T2	0.83 ± 0.06	0.73 ± 0.11	*
		VSMTY	FLAIR	**0.94 ± 0.06**	0.79 ± 0.12	**
			T2	0.91 ± 0.07	0.86 ± 0.12	*
		AVGHD	FLAIR	**0.33 ± 0.26**	1.98 ± 1.62	**
			T2	0.35 ± 0.19	1.6 ± 1.40	*
	2	DICE	FLAIR	**0.85 ± 0.07**	0.68 ± 0.18	*
			T2	0.83 ± 0.06	0.70 ± 0.09	**
		VSMTY	FLAIR	**0.94 ± 0.06**	0.75 ± 0.79	*
			T2	0.91 ± 0.07	0.80 ± 0.13	*
		AVGD	FLAIR	**0.33 ± 0.26**	2.04 ± 1.70	*
			T2	0.35 ± 0.19	1.29 ± 1.21	*
	3	DICE	FLAIR	**0.85 ± 0.07**	0.071 ± 0.10	**
			T2	0.83 ± 0.06	0.62 ± 0.14	**
		VSMTY	FLAIR	**0.94 ± 0.06**	0.81 ± 0.10	**
			T2	0.91 ± 0.07	0.76 ± 0.21	*
		AVGHD	FLAIR	**0.33 ± 0.26**	1.81 ± 1.22	**
			T2	0.35 ± 0.19	2.85 ± 2.29	**

Table 2

Comparison with related algorithms for brain tumor segmentation from BRATS database.

Algorithms	Average Dice score		Time (min) (architecture)	Segmentation type
	HG	LG		
Cordier et al. [8]	0.79 ± 0.87	0.76 ± 0.18	20(Cluster)	Supervised learning
Festa et al. [13]	0.83 ± 0.08	0.7 ± 0.17	30 (CPU)	Supervised learning
Guo et al. [16]	0.82 ± 0.12	–	1 (CPU) + User interaction	Semi - supervised
Meier et al. [27]	0.80 ± 0.12	0.76 ± 0.11	6 (CPU)	Supervised learning
Zhao et al. [44]	0.83 ± 0.99	0.83 ± 0.93	20 (CPU)	Supervised learning
SGC [36]	0.78 ± 0.09	0.73 ± 0.11	2 (CPU) + User interaction	Semi - supervised
AGC	**0.86 ± 0.06**	**0.85 ± 0.07**	**2 (CPU)**	**Automated**

4. Conclusions and discussion

We have developed a novel scheme for automated GBM tumor detection and segmentation from multi-channel brain MR images using saliency. Results were provided over the largest public dataset available, from the *BRATS 2013 challenge*, and comparative analysis obtained w.r.t several related state-of-the-art brain tumor segmentation methods. Typically brain tumor segmentation is a difficult task for humans [28], with "currently available algorithms reaching Dice scores of around 80% for whole tumor segmentation". Our algorithm AGC, producing a Dice score of 86%, is thereby indicative of superior performance.

The saliency detection method being based on the concept of pseudo-coloring, helped in suppressing the less relevant regions while enhancing the salient parts. The resulting saliency maps were validated with respect to the ground truths provided by the experts. The AUC score in the ROC analysis was found to range between $0.98 ± 0.015$ in the high-grade cases and $0.99 ± 0.004$ in the low-grade cases, on an average, which is very high and provides as good a prediction of the tumor location as human experts.

The segmentation accuracy of the semi-automatic segmentation like Grow-Cut (SGC) is dependent on the placement of initial seed regions, selection of appropriate slices for marking, as well as the number of initial slices chosen by the observer. Here human interaction and interpretation of medical images is still a considerable source of variation. Furthermore, slice-by-slice manual contouring of two-dimensional images is a time consuming process. Our automated Grow-Cut (AGC) can efficiently overcome these drawbacks. It was observed that the segmentation produced by AGC had significantly higher accuracy (with maximum error of 0.2) as compared to the manual method, and performed better than the state-of-the-art algorithms, using semi-supervised or supervised learning.

Inter-observer variability of semi-automated methods like SGC was found to be particularly high for low-grade gliomas, which are typically more difficult to segment and result in deviating expert opinions. Automated segmentation is more robust to such variation because it does not involve user intervention. Semi-automated methods, on the other hand, require initial selection of seed points; which is difficult due to imaging artifacts like partial volume effect.

A major drawback of the supervised or semi-supervised segmentation methods is the user interaction time, which makes these unsuitable for daily clinical practice. Moreover supervised training based segmentation requires either a complex prior model or a large amount of training data for generating satisfactory results, along with larger computational time and resources during training. Our AGC requires neither a large amount of training data or supervision, nor a powerful and expensive workstation or clusters. The computing time, with an Intel Core $i7 - 2600\,K$, 3.40 GHz processor having 16GB memory system, was about 2 min for each case (per patient). A real-time realization of the algorithm can be achieved with a *GPU* based implementation, thereby enhancing its clinical applicability.

Acknowledgment

References

[1] R. Achanta, F. Estrada, P. Wils, S. Süsstrunk, Salient region detection and segmentation, in: Computer Vision Systems, Springer, 2008, pp. 66–75.
[2] S. Alpert, P. Kisilev, Unsupervised detection of abnormalities in medical images using salient features, in: SPIE Medical Imaging, International Society for Optics and Photonics, 2014, pp. 903416–903421.
[3] S. Banerjee, S. Mitra, B. Uma Shankar, Single seed delineation of brain tumor using multi-thresholding, Inf. Sci. 330 (2016) 88–103.
[4] P. Bian, L. Zhang, Biological plausibility of spectral domain approach for spatiotemporal visual saliency, in: Advances in Neuro-Information Processing, Springer, 2009, pp. 251–258.
[5] F. Binczyk, B. Stjelties, C. Weber, M. Goetz, K. Meier-Hein, H.-P. Meinzer, R. Bobek-Billewicz, R. Tarnawski, J. Polanska, Mimseg-an algorithm for automated detection of tumor tissue on NMR apparent diffusion coefficient maps, Inf. Sci. 384 (2017) 235–248.
[6] A. Borji, L. Itti, State-of-the-art in visual attention modeling, IEEE Trans. Pattern Anal. Mach. Intell. 35 (2013) 185–207.
[7] A. Borji, C. Ming-Ming, J. Huaizu, L. Jia, Salient object detection: a benchmark, IEEE Trans. Image Process. 24 (2015) 5706–5722.
[8] N. Cordier, B. Menze, H. Delingette, N. Ayache, Patch-based segmentation of brain tissues, in: NCI-MICCAI Challenge on Multimodal Brain Tumor Segmentation: Proc.NCI-MICCAI BRATS 2013, IEEE, 2013, pp. 6–17.
[9] K.S. Deepak, A. Chakravarty, J. Sivaswamy, et al., Visual saliency based bright lesion detection and discrimination in retinal images, in: 10th IEEE International Symposium on Biomedical Imaging, IEEE, 2013, pp. 1436–1439.
[10] J. Egger, et al., GBM volumetry using the 3D Slicer medical image computing platform, Sci. Rep. 3 (2013) 1364–1371.
[11] E. Erdem, A. Erdem, Visual saliency estimation by nonlinearly integrating features using region covariances, J. Vis. 13 (2013) 11.
[12] M. Erihov, S. Alpert, P. Kisilev, S. Hashoul, A cross saliency approach to asymmetry-based tumor detection, in: Medical Image Computing and Computer-Assisted Intervention MICCAI 2015, in: Lecture Notes in Computer Science, 9351, Springer International Publishing, 2015, pp. 636–643.
[13] J. Festa, S. Pereira, J.A. Mariz, N. Sousa, C.A. Silva, Automatic brain tumor segmentation of multi-sequence MR images using random decision forests, in: NCI-MICCAI Challenge on Multimodal Brain Tumor Segmentation: Proc.NCI-MICCAI BRATS 2013, IEEE, 2013, pp. 23–26.
[14] T. Foulsham, G. Underwood, What can saliency models predict about eye movements? Spatial and sequential aspects of fixations during encoding and recognition, J. Vis. 8 (2008) 1–17.
[15] R.A. Gatenby, O. Grove, R.J. Gillies, Quantitative imaging in cancer evolution and ecology, Radiology 269 (2013) 8–14.
[16] X. Guo, L. Schwartz, B. Zhao, Semi-automatic segmentation of multimodal brain tumor using active contours, in: NCI-MICCAI Challenge on Multimodal Brain Tumor Segmentation: Proc.NCI-MICCAI BRATS 2013, IEEE, 2013, pp. 27–30.
[17] J. Harel, C. Koch, P. Perona, Graph-based visual saliency, in: Advances in Neural Information Processing Systems, 2006, pp. 545–552.
[18] E.C. Holland, Glioblastoma multiforme: the terminator, Proc. Natl. Acad. Sci. 97 (2000) 6242–6244.
[19] Q. Huang, F. Yang, L. Liu, X. Li, Automatic segmentation of breast lesions for interaction in ultrasonic computer-aided diagnosis, Inf. Sci. 314 (2015) 293–310.
[20] L. Itti, C. Koch, E. Niebur, A model of saliency-based visual attention for rapid scene analysis, IEEE Trans. Pattern Anal. Mach. Intell. 20 (1998) 1254–1259.
[21] A.K. Jain, Fundamentals of Digital Image Processing, 3, Prentice-Hall, Englewood Cliffs, 1989.
[22] V. Jampani, J. Sivaswamy, V. Vaidya, et al., Assessment of computational visual attention models on medical images, in: Proceedings of the Eighth Indian Conference on Computer Vision, Graphics and Image Processing, ACM, 2012, p. 80.
[23] H. Khotanlou, O. Colliot, J. Atif, I. Bloch, 3D brain tumor segmentation in MRI using fuzzy classification, symmetry analysis and spatially constrained deformable models, Fuzzy Sets Syst. 160 (10) (2009) 1457–1473.
[24] M. Kistler, S. Bonaretti, M. Pfahrer, R. Niklaus, P. Büchler, The virtual skeleton database: an open access repository for biomedical research and collaboration, J. Med. Internet Res. 15 (11) (2013) e245.
[25] H. Li, T. Han, J. Wang, Z. Lu, X. Cao, Y. Chen, L. Li, C. Zhou, X. Chai, A real-time image optimization strategy based on global saliency detection for artificial retinal prostheses, Inf. Sci. 415–416 (2017) 1–18.
[26] Y.-F. Ma, H.-J. Zhang, Contrast-based image attention analysis by using fuzzy growing, in: Proceedings of the Eleventh ACM International Conference on Multimedia, ACM, 2003, pp. 374–381.
[27] R. Meier, S. Bauer, J. Slotboom, R. Wiest, M. Reyes, A hybrid model for multimodal brain tumor segmentation, in: NCI-MICCAI Challenge on Multimodal Brain Tumor Segmentation: Proc.NCI-MICCAI BRATS 2013, IEEE, 2013, pp. 31–37.
[28] B. Menze, et al., The multimodal brain tumor image segmentation benchmark (BRATS), IEEE Trans. Med. Imaging 34 (2014) 1993–2024.
[29] S. Mitra, B. Uma Shankar, Medical image analysis for cancer management in natural computing framework, Inf. Sci. 306 (2015) 111–131.

[30] C. Parmar, E.R. Velazquez, R. Leijenaar, M. Jermoumi, S. Carvalho, R.H. Mak, S. Mitra, B. Uma Shankar, Robust radiomics feature quantification using semiautomatic volumetric segmentation, PLoS ONE 9 (2014) e102107.

[31] G. Quellec, S.R. Russell, M.D. Abramoff, Optimal filter framework for automated, instantaneous detection of lesions in retinal images, IEEE Trans. Med. Imaging 30 (2011) 523–533.

[32] P.L. Rosin, A simple method for detecting salient regions, Pattern Recognit. 42 (2009) 2363–2371.

[33] B.N. Saha, N. Ray, R. Greiner, A. Murtha, H. Zhang, Quick detection of brain tumors and edemas: a bounding box method using symmetry, Comput. Med. Imaging Graph. 36 (2) (2012) 95–107.

[34] M. Song, C. Chen, S. Wang, Y. Yang, Low-level and high-level prior learning for visual saliency estimation, Inf. Sci. 281 (2014) 573–585.

[35] S. Ullman, A. Sha'ashua, Structural saliency: the detection of globally salient structures using a locally connected network, in: Proceedings of the Second International Conference on Computer Vision, 1988, pp. 321–327.

[36] V. Vezhnevets, V. Konouchine, GrowCut: interactive multi-label ND image segmentation by cellular automata, in: Graphicon, 2005, pp. 150–156.

[37] D. Walther, C. Koch, Modeling attention to salient proto-objects, Neural Netw. 19 (2006) 1395–1407.

[38] Y. Yang, M. Song, N. Li, J. Bu, C. Chen, What is the chance of happening: a new way to predict where people look, in: Computer Vision–ECCV 2010, 2010, pp. 631–643.

[39] J. Yu, Y. Rui, B. Chen, Exploiting click constraints and multi-view features for image re-ranking, IEEE Trans. Multimed. 16 (1) (2014) 159–168.

[40] J. Yu, D. Tao, J. Li, J. Cheng, Semantic preserving distance metric learning and applications, Inf. Sci. 281 (2014) 674–686.

[41] J. Yu, D. Tao, M. Wang, Adaptive hypergraph learning and its application in image classification, IEEE Trans. Image Process. 21 (7) (2012) 3262–3272.

[42] L. Zhang, M.H. Tong, T.K. Marks, H. Shan, G.W. Cottrell, Sun: a Bayesian framework for saliency using natural statistics, J. Vis. 8 (2008) 32.

[43] Y. Zhang, Z. Mao, J. Li, Q. Tian, Salient region detection for complex background images using integrated features, Inf. Sci. 281 (2014) 586–600.

[44] L. Zhao, D. Sarikaya, J.J. Corso, Automatic brain tumor segmentation with MRF on supervoxels, in: MICCAI Challenge on Multimodal Brain Tumor Segmentation, IEEE, 2013, pp. 51–54.

[45] P.O. Zinn, P. Sathyan, B. Mahajan, J. Bruyere, M. Hegi, S. Majumder, R.R. Colen, A novel Volume-Age-KPS (VAK) Glioblastoma classification identifies a prognostic cognate microRNA-gene signature, PLoS ONE 7 (2012) e41522.